Surface-based inversions above central Greenland

N. B. Miller,[1] D. D. Turner,[2] R. Bennartz,[3] M. D. Shupe,[4] M. S. Kulie,[1]
M. P. Cadeddu,[5] and Von P. Walden[6]

Received 17 September 2012; revised 26 November 2012; accepted 28 November 2012; published 30 January 2013.

[1] Surface-based temperature inversions (SBIs) are studied at Summit Station in central Greenland during the period spanning July 2010 to May 2012. The frequency and intensity of SBI are examined using microwave radiometer (MWR) temperature retrievals, radiosonde profiles, and near-surface meteorological data. Using the MWRs' high temporal resolution, the diurnal, monthly, and annual cycles are investigated. Monthly mean values in SBI occurrence and intensity show that surface-based inversions are prevalent in the winter with decreasing values in the summer months. A case study on 20 February 2011 suggests that factors other than solar elevation angle influence the intensity of surface-based inversions. An increase in liquid water path corresponds to a decrease in SBI intensity, suggesting that liquid-bearing clouds, especially within the lowest 1 km, are associated with weaker surface-based inversions.

Citation: Miller, N. B., D. D. Turner, R. Bennartz, M. D. Shupe, M. S. Kulie, M. P. Cadeddu, and V. P. Walden (2013), Surface-based inversions above central Greenland, *J. Geophys. Res. Atmos.*, *118*, 495–506, doi:10.1029/2012JD018867.

1. Introduction

[2] The growth or decline of the Greenland Ice Sheet (GIS) is dependent on the atmospheric state, which provides the context for the dynamical processes that transfer energy and mass to and from the surface. By investigating the interface between the free atmosphere and the surface, many factors contributing to GIS change can be understood. The temperature as a function of height above the surface is an indicator of the stability of the boundary layer. Stability inhibits mixing and decouples the surface from elevated features, such as clouds, while an unstable profile gives rise to a surface mixed layer, which contains turbulent mixing of surface mass and heat. Hence, characterizing the stability of the lower troposphere is useful when investigating the atmospheric boundary layer above the GIS.

[3] Surface-based temperature inversions (SBI) are a dominant feature over the GIS because the highly reflective surface absorbs little direct sunlight, while the highly emissive surface radiatively cools to space. These inversions are characterized by temperatures increasing with altitude to the top of the inversion layer and were observed in the Arctic nearly a century ago by *Sverdrup* [1926]. In dry conditions, the radiative cooling of the surface also has the potential to cool elevated layers of the atmosphere, resulting in deep inversions [*Bradley and Keimig*, 1992]. Climatological modeling efforts show up to 80% mean annual SBI frequency over the center of the GIS with increased depth and intensity in the winter [*Zhang et al.*, 2011].

[4] *Zhang et al.* [2011] also shows that modeled estimates of summer SBI frequency can be highly discrepant above central Greenland, differing by up to 20%–30%. Insights into the radiative and atmospheric processes that lead to changes in the boundary layer structure can be used to improve modeling efforts, helping to explain and predict GIS change. The downwelling longwave radiative contribution is an important consideration because GIS change is dependent on the surface energy budget: a balance of the incoming and outgoing radiation versus the sensible and latent heat fluxes. During cloudy scenes, the effect of the downwelling longwave radiation on the surface and SBIs is not certain, although radiosonde data from Alaska point to a correlation between weak, shallow SBIs and large liquid water path (LWP) values [*Bourne*, 2008]. A case study by *Hudson and Brandt* [2005] suggests that the increase in downward longwave flux from clouds warms the surface and weakens the temperature inversion.

[5] "An Integrated Characterization of Energy, Clouds, Atmospheric state, and Precipitation at Summit" (ICECAPS), a project funded by the National Science Foundation, is collecting a multi-instrument, multi-year dataset to develop a comprehensive picture of the atmosphere over the GIS. This field campaign, located at Summit Greenland (elevation of 3255 m at 72° 35'N and 38° 25'W), aims to improve the understanding of basic atmosphere and cloud processes. Combining atmospheric state information with cloud property information allows for a better understanding of the impact of various types of clouds on the radiation balance and surface mass budget. Mixed-phase clouds,

[1]Space Science and Engineering Center, University of Wisconsin, Madison, Wisconsin, USA.
[2]National Severe Storms Laboratory, NOAA, Norman, Oklahoma, USA.
[3]Department of Atmospheric and Oceanic Sciences, University of Wisconsin, Madison, Wisconsin, USA.
[4]Cooperative Institute for Research in Environmental Sciences, University of Colorado and NOAA, Boulder, Colorado, USA.
[5]Argonne National Laboratory, DOE Lemont, Illinois, USA.
[6]Department of Geography, University of Idaho, Moscow, Idaho, USA.

Corresponding author: N. B. Miller, Space Science and Engineering Center, University of Wisconsin, 1225 W. Dayton Street, Madison, WI 53706, USA. (nate.miller@ssec.wisc.edu)

©2012. American Geophysical Union. All Rights Reserved.
2169-897X/13/2012JD018867

which occur frequently over many Arctic sites including Summit, pose a unique challenge in their difficulty to model and observe [*Shupe et al.,* 2008]. The ground-based station at Summit is able to provide valuable insight into which parameterizations are valid and the processes that create and maintain various types of mixed-phase clouds. This unique Summit dataset will be used to improve the modeling of various atmospheric processes, improve forecast accuracy, and produce precise measurements for ground validation of satellite overpasses. A comprehensive description of the ICECAPS project is given by *Shupe et al.* [2013].

[6] ICECAPS' instruments are integrated to provide complementary measurements of many geophysical variables, thus providing cross calibration and redundancy in case of individual instrument issues. For example, temperature profiles (T[z]) are observed using twice daily radiosondes and can be retrieved from microwave radiometer (MWR) brightness temperature observations. Moisture content, including liquid water path (LWP) and precipitable water vapor (PWV), can also be retrieved from the MWR dataset, which includes higher-frequency observations at 90 and 150 GHz to enhance sensitivity to small amounts of LWP. Cloud macrophysics, including occurrence and location, are measured by a ceilometer.

[7] This paper characterizes the surface-based inversions (SBIs) that often occur at Summit and investigates the correlation between the SBI intensity with factors such as liquid-bearing clouds. Data from July 2010 to May 2012 are used to examine SBI variability (frequency and intensity) during the diurnal, monthly, and annual cycle, as well as how the SBI is modified by cloud properties. Atmospheric properties obtained via the MWRs, which include temperature as a function of height, are compared to radiosonde profiles and near-surface meteorological data.

2. Methodology

2.1. Forward Model

[8] The monochromatic radiative transfer model, MonoRTM v4.2, distributed by Atmospheric and Environmental Research, Inc., is utilized to compare modeled brightness temperatures (Tb) to calibrated MWR brightness temperatures [*Clough et al.*, 2005].The line parameters are based on the HITRAN 2004 database with improvements in line width, strength, and coupling for oxygen and water vapor lines [*Payne et al.,* 2011]. The MonoRTM model uses the MT_CKD (v2.4) continuum model [*Mlawer et al.*, 2012]. The liquid water absorption model used by MonoRTM is from *Liebe et al.* [1991].

2.2. Direct Measurements

[9] Direct measurements of the temperature profile above Summit are recorded by Vaisala RS92 radiosondes. The radiosonde profiles contain high vertical resolution yet are limited to the twice daily (1115 and 2315 UTC) launch times. A near-surface meteorological tower, maintained by the National Oceanic and Atmospheric Administration's Global Monitoring Division, records temperature at two discrete levels (2m and 10m), with a temporal resolution on the order of seconds. The radiosonde profile uses the tower's 2m data as input for the surface temperature value. The specified resolution of the radiosonde and tower temperature sensors are both 0.1°C.

2.3. MWR Retrievals

2.3.1. Microwave Radiometers

[10] ICECAPS has positioned two MWRs, both of which were built by Radiometer Physics GmbH (RPG), on the roof of the Mobile Science Facility at Summit. These passive instruments are ideal for providing continuous data with a temporal resolution on the order of seconds. The Humidity and Temperature Profiler (HATPRO) has two receiver units that are designed to be thermally stable to within 0.03 K [*Rose and Czekala*, 2009; *Rose et al.*, 2005]. In this analysis, the HATPRO frequencies utilized in the retrievals include two K-band channels (23.84 and 31.40 GHz) and six V-band channels (52.28, 53.86, 54.94, 56.66, 57.30, and 58.00 GHz). The high-frequency (HF) radiometer is a separate MWR that is synchronized to the HATPRO through software and provides two additional channels at 90 and 150 GHz, both of which are also used in this analysis.

[11] A majority of the time the scene mirrors are pointing toward zenith with a 2 second integration time, yet the MWRs also record elevation scans on either side of zenith. The elevation scan is composed of the following seven angles on each side of zenith:

$$5.4^\circ \quad 10.2^\circ \quad 16.2^\circ \quad 19.2^\circ \quad 23.4^\circ \quad 30.0^\circ \quad 42.0^\circ \quad 90.0^\circ$$

[12] The elevation angles above 20° on both sides of zenith are analyzed as a "tip calibration" [*Han and Westwater*, 2000] in clear sky conditions using an algorithm similar to *Liljegren* [2000]. A tip calibration produces values of the system temperature, gain, and the effective temperature of the noise diode in the transparent K-band channels and for the 90 and 150 GHz channels. The effective temperature of the noise diodes in each of the V-band channels was calibrated using an external target filled with liquid nitrogen placed on the side of the HATPRO MWR.

[13] The Summit location is a physically demanding environment with temperatures reaching below the suggested MWRs' operating range (–30°C to +45°C, *Rose and Czekala* [2009]). If the environmental temperature is too cold, the receiver's electronics are unable to thermally stabilize, causing issues with the automatic calibration. Over the 2010–2011 winter, there were times when the MWR was unable to maintain thermal stability. On 16 August 2011, a 1.5 inch piece of rigid foam insulation was inserted between the stand and the MWR for both the HATPRO and HF. Insulation was also clamped to a wooden frame to blanket the MWR housing while tightly covering the side vents. These actions helped to thermally stabilize the MWRs and increase the operational time. Figure 1 shows the percentage of time each radiometer was operational and produced acceptable data, from 13 July 2010 through 31 May 2012. The statistics in Figure 1 include a period from 5 October 2010 to 30 December 2010 where the data were unusable because the scene mirror slipped on the rotating axis in the HATPRO.

2.3.2. LWP and PWV

[14] A physical retrieval of LWP and PWV, called MWRRET, was implemented similar to *Turner et al.* [2007].

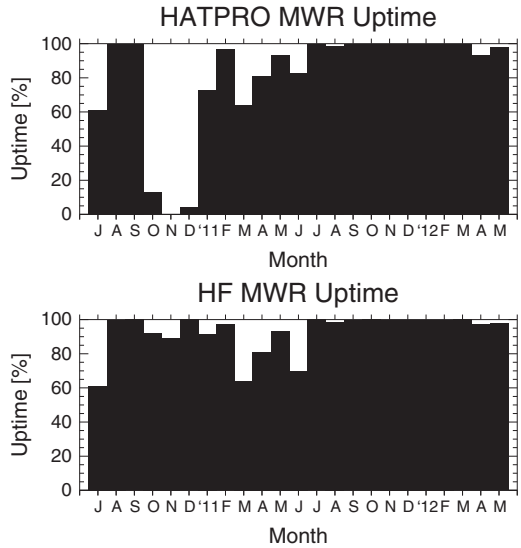

Figure 1. The percentage of time the HATPRO (top) and HF (bottom) microwave radiometers were operational with good quality data from July 2010 to May 2012.

MWRRET employs four frequencies: 23.8, 31.4, 90.0, and 150.0 GHz. The HF radiometer provides increased sensitivity to LWP and PWV *Crewell and Löhnert* [2003]. MWRRET provides uncertainty estimates for each retrieval. The mean PWV uncertainty is 0.3 mm, and the LWP uncertainty is on the order of 3 g/m^2; thus, we will use a threshold of 5 g/m^2 to identify cases that have liquid-bearing clouds.

2.3.3. Tb Bias Correction

[15] *Löhnert and Maier* [2012] show that correcting for the bias between the observed brightness temperatures and those computed from the MonoRTM leads to decreased amounts of bias and error in retrieved values. Hence, this technique, for clear sky scenes, is applied to the MWR temperature retrieval. If the standard deviation of the 90 GHz Tb observations, in a 20 minute window, is less than 0.25°C, then the period is considered clear sky. The clear sky results for the 23.84, 31.40, 90.0, and 150.0 GHz channels are shown in the top 4 panels of Figure 2.

[16] The bottom six panels of Figure 2 show the bias of the six operational V-band brightness temperatures. This bias in the V-band channels appears to be dependent upon the annual cycle as well as the LN2 calibration period (i.e., changes after the LN2 calibration) and thus is likely due in part to errors in the calibration. A full evaluation of LN2 calibration uncertainties is provided by *Maschwitz et al.* [2013]. *Cadeddu et al.* [2007] describes how improvements in oxygen line-parameter modeling, applied to MonoRTM, have more accurately described the temperature dependence of the width and mixing coefficients. Despite these improvements, subtle effects may linger at these very dry conditions, especially at the lower pressure conditions observed at Summit, leading to the change in bias for cold surface temperatures as seen in Figure 3.

[17] Distinct corrections are estimated for three different periods (indicated by two of the vertical lines in Figure 2): before the 16 June 2011 LN2 calibration (first solid line), between the June calibration and when the insulation was added on 16 August 2011 (dashed line), and finally after 16 August 2011. A linear function is used to fit the clear sky biases as a function of temperature, thus capturing the slopes seen in Figure 3 for each period. Hence, a known surface temperature is used to estimate the bias correction needed to match the observed Tb to the modeled value. A bias correction of the off-zenith measurements is performed in the same manner by fitting the same clear sky cases.

2.3.4. Temperature Profiles

[18] The MWR retrievals are performed every 40 minutes (i.e., the frequency of the elevation scans), providing middle ground regarding the trade-off between temporal and vertical resolution. A statistical temperature retrieval using the V-band Tb observations was developed using a training set of temperature profiles consisting of NOAA ozonesonde measurements at Summit from 2005 to 2010, along with ICECAPS radiosondes from the period May 2010 to June 2011 (total of 998 soundings). The retrieval uses 105 altitude levels starting at the surface (3255 m MSL), with fine vertical spacing near the surface and increasing to 50 m aloft: 0, 10, 20, 35, 55, 80, 110, 150, 200, 250, . . .4950, and 5000 m above ground level. Since using off-zenith angles greatly improves the vertical resolution and accuracy of the retrieved temperature profile [*Crewell and Löhnert*, 2007], profiles of temperature are retrieved using off-zenith and zenith observations simultaneously. Evoking linear regression techniques, quadrature coefficients (c_{ij}) are optimized such that the temperature at a level (T_i) is estimated by utilizing 48 channels (Tb_j) consisting of 6 frequencies at 8 different elevation angles [*Twomey*, 1977].

[19] The retrieval must be developed to ensure error is not introduced since these 48 Tb observations likely have similar information content. By performing a principal component analysis and then retaining only the principal components that describe signal (as described in the study by *Turner et al.* [2006]), the inversion error can be reduced. Using the modeled brightness temperatures from the 998 soundings, the optimal number of principal components to use in the temperature retrieval was found to be 13.

[20] The process of determining 48 retrieval coefficients from 13 principal components is performed at all 105 levels. For each level, the mean temperature ($\bar{T}_i$) as well as the mean brightness temperatures ($\bar{Tb}_j$) are subtracted from the corresponding sounding values resulting in 998 equations and 48 unknowns.

$$T_i - \bar{T}_i = \sum_{j=1}^{48} c_{ij}\left(Tb_j - \bar{Tb}_j\right) \tag{1}$$

[21] To determine the coefficients (c_{ij}), representative random noise is added to the simulated brightness temperatures, before subtracting the mean value. Then singular value decomposition is performed on the 48×998 array ($Tb_j + noise - \bar{Tb}_j$), producing a set of three arrays: a 48×998 orthogonal array of eigenvectors (U), a second 48×48 diagonal array with 48 corresponding eigenvalues (W), and a third 48×48 orthogonal array (Z). The eigenvalues are reordered in descending order before truncating the arrays that represent

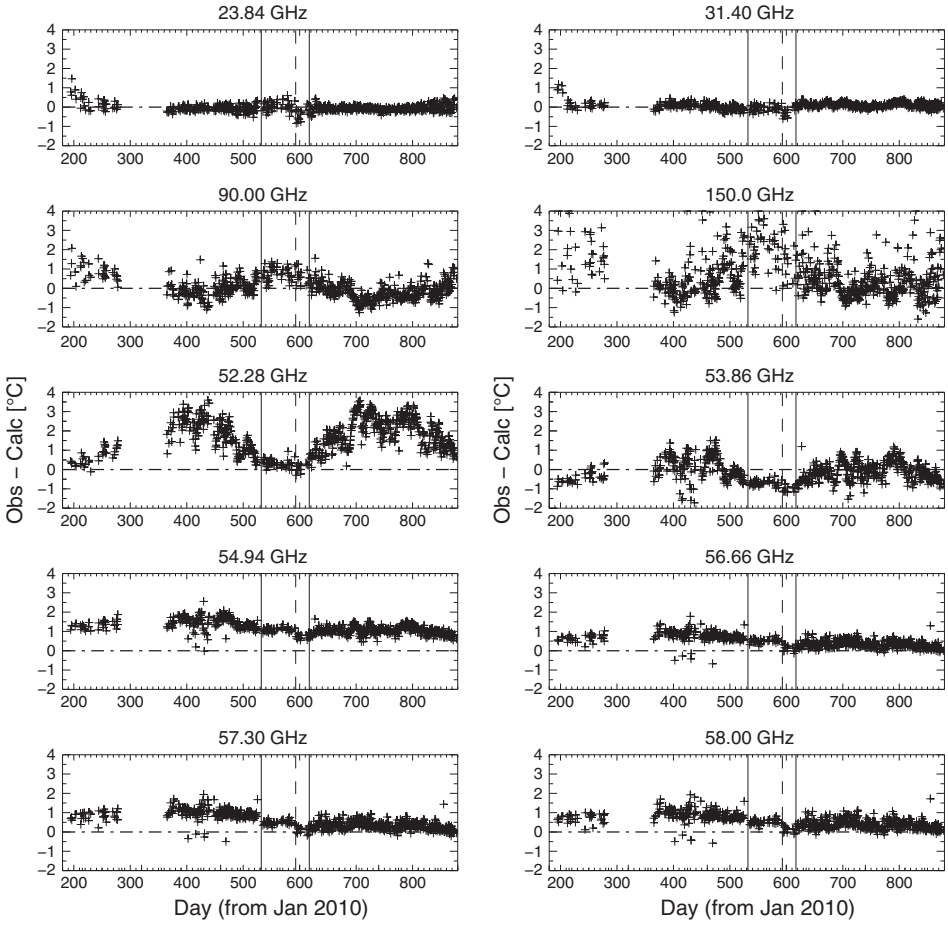

Figure 2. Average calibrated MWR brightness temperatures (obs), over a 20 minute window, minus modeled brightness temperatures (calc) for the 10 channels used in this study. Only clear sky cases are shown as determined by the standard deviation of the 90 GHz channel. Solid vertical lines indicate an LN2 calibration, and the dashed vertical line is when the insulation was installed on the radiometers to improve their thermal stability in the cold environment.

the optimal number of principal component channels (13). Coefficients are determined via back substitution techniques while truncating the U, W, and Z arrays to 13×998, 13×13, and 13×48 elements, respectively.

[22] Figure 4 shows that implementing the brightness temperature corrections (Section 2.3.3) reduce the root mean square (RMS) differences between the radiosonde and MWR retrieved temperature profiles. There is a large reduction in the bias values as well. The RMS error at the surface is largely due to representativeness error of the different sensor locations and to turbulence near the surface [*Löhnert and Maier*, 2012]. From 1 to 5 km, there are only 1.8 degrees of freedom of signal spread out over 4 km (see section 2.3.5) explaining the increased RMS error above 1 km. Thus, temperature structures above 1 km are difficult to resolve using the MWR retrievals.

2.3.5. Resolution of T[z]

[23] Due to the limitations of using a passive radiometer in the retrieval process (i.e., due to the broadening of the weighting functions with distance away from the instrument), the retrieved profile will be a vertically smoothed function of the true profile. The averaging kernel describes the resolution and information content of the retrieval in a quantitative manner. Using the framework described in *Rodgers* [2000], 25 cases over the course of the year are investigated to quantify the information content at each level. The Jacobian (K) describes the sensitivity of the forward model to the state of the atmosphere. The averaging kernel (A) can then be calculated by also including the uncertainty in the observations (S_m) and the covariance of the set of radiosonde soundings which includes data ± 2 months from the retrieved profile (S_a).

$$A = \left(S_a^{-1} + K^T S_m^{-1} K\right)^{-1} K^T S_m^{-1} K \tag{2}$$

[24] The uncertainty in the V-band observations is assumed to be uncorrelated and equal to 0.5°C in the first three channels (i.e., 52.3, 53.9, 54.9 GHz) and 0.3°C in the last three channels (i.e., 56.7, 57.3, 58.0 GHz).

[25] The total degrees of freedom for signal are given by the trace of the averaging kernel matrix. The mean value of the 25 representative cases was 5 degrees of freedom for signal over all 105 levels. The vertical resolution at each level can be determined by considering the shape and amplitude of the averaging kernel at that level, often referred to as the smoothing function [*Rodgers*, 2000]. Figure 5 shows the mean widths and amplitudes of the smoothing functions for the 25 representative cases below 3 km. The surface

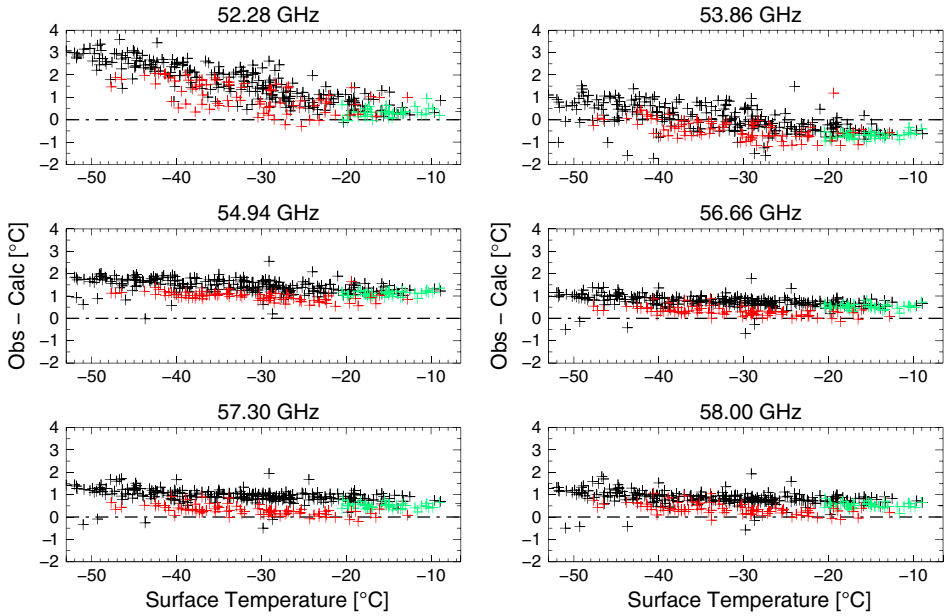

Figure 3. Calibrated MWR brightness temperatures (obs) minus modeled brightness temperatures (calc) for the six channels used in the statistical temperature retrieval as a function of surface temperature. Only clear sky cases are shown as determined by the standard deviation of the 90 GHz channel. Black points are before the 16 June 2011 calibration, green points are after this calibration and before the insulation was added on 16 August 2011, and the red are the points after the insulation was added.

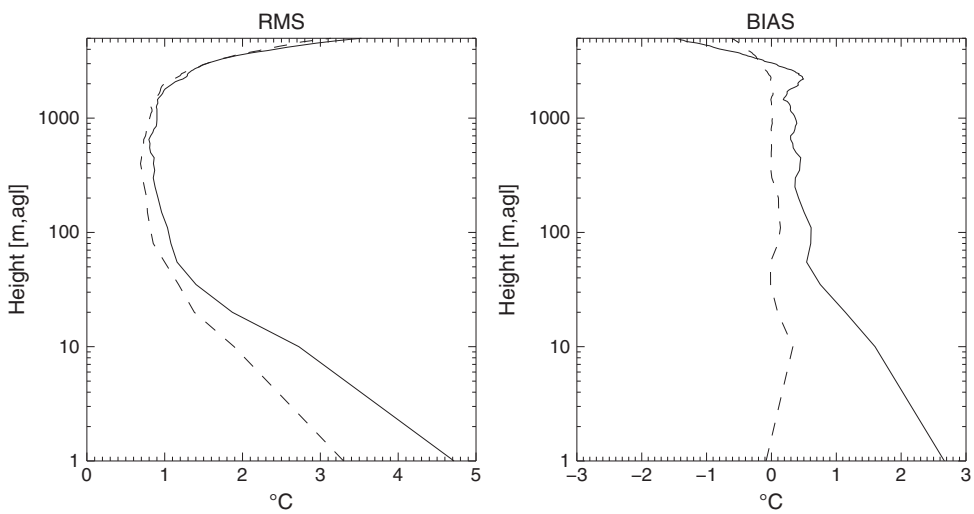

Figure 4. Root mean square (RMS) difference and bias values of the MWR statistical temperature profile retrievals relative to radiosondes that are within half an hour from the sounding launch time. The RMS (left panel) and bias (right panel) values are shown for the corrected V-band brightness temperatures (dashed line) and for the temperature retrieval values obtained using the original brightness temperatures (solid line).

level has the highest information content (amplitude = 0.873). The lowest 10, 500, 1000, 2000, and 3000 m above the surface contain 1.1, 2.7, 3.2, 3.7, and 4.1 degrees of freedom of the signal, respectively; thus, the information content is largely located near the surface and drops off quickly with altitude. Although the shape of the smoothing function is not well defined at the edges of the averaging kernel matrix, the vertical resolution of the temperature profiles can be estimated and was found to be on the order of a hundred meters for the lower levels before increasing by over an order of magnitude above 1 km. Likewise, estimates provided by *Cadeddu et al.* [2002] for similar retrieval techniques place the vertical resolution at 80–100 m for the detection of a surface-based inversion with intensity ≥ 1°C.

2.4. Surface-Based Inversion Criteria

[26] Radiosonde profiles, MWR-retrieved temperature profiles, and near-surface meteorological data are used to characterize surface-based inversions at Summit. For the

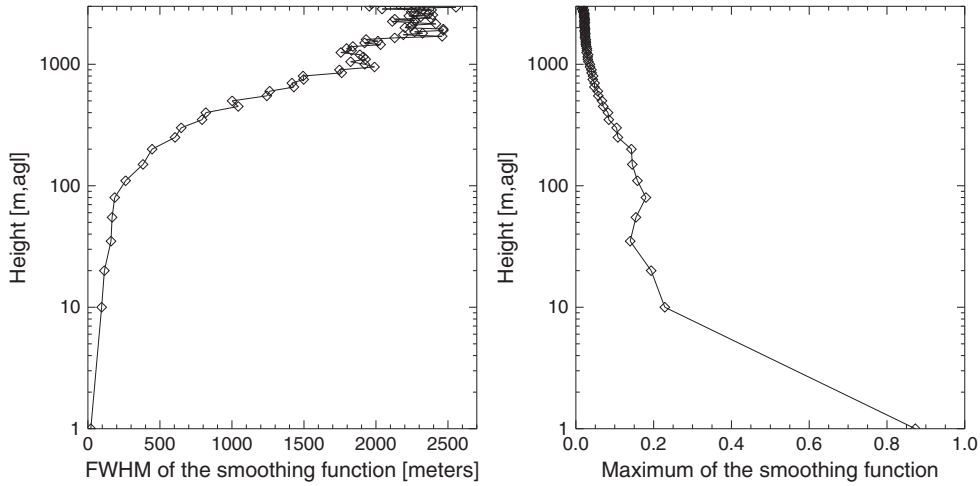

Figure 5. The average width (left panel) and maximum value (right panel) of the smoothing function at each level of the temperature profile retrieval, using the averaging kernel for 25 cases over a range of conditions.

radiosonde and MWR profiles, a spline fit is implemented at 1 m resolution. The base of the inversion is defined to be where the temperature begins to increase with altitude and is less than the temperature at 40 m above this level. The top of the inversion is defined to be the altitude where the temperature begins to decrease with increasing altitude and remains greater than the temperature at 40 m above this level. The intensity is defined as the difference of the temperature at the top of the inversion and the temperature at the base, similar to that of *Zhang et al.* [2011]. If the temperature profile does not increase with elevation over the 40 m window, then the profile is not considered an inversion. If the base is located at the surface, the inversion is considered surface-based. The 10 and 2 m tower-based meteorological data are subtracted to provide a direct measurement of the temperature difference between these levels.

[27] Using error estimates from direct and indirect measurements, a minimum threshold for intensity is determined to be considered an inversion. Requiring that the radiosonde and tower-derived intensities be $\geq 0.2°C$ reduces the possibility of measurement error incorrectly identifying an inversion. The RMS error profile (Figure 4, left panel) is used to set the threshold for identifying cases with inversions from the MWR-retrieved profiles. Since the RMS error is below 1°C from 100 to 1000 m, a threshold of 2°C is used to identify inversions in the MWR data.

3. Results

3.1. Surface-Based Inversions

[28] The upper panel in Figure 6 shows the monthly percentage of inversions, derived from the MWR retrieved

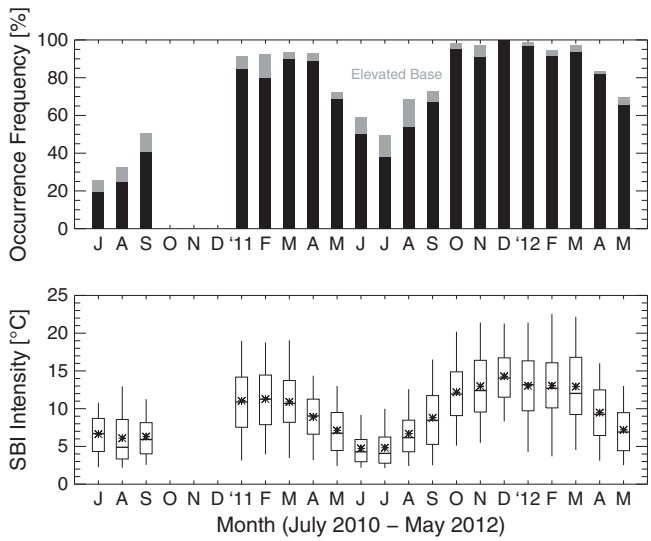

Figure 6. Percentage of MWR surface-based (black) and elevated base (gray) inversions (top panel) and monthly statistics of surface-based inversion intensities (lower panel). Surface-based inversions have a base at the surface and an intensity greater than 2°C. For the box-and-whisker plots in the lower panel, the box indicates the 25th and 75th percentiles, the whiskers indicate the 5th and 95th percentiles, the middle line is the median, and the asterisk indicates the mean.

profiles, from July 2010 to May 2012. The occurrence frequencies for both surface-based inversions (black) and inversions with an elevated base (>0 m; gray) are given. Of 19,999 quality-controlled temperature profiles, a total of 78% had an inversion present, and 72% of all the profiles had a surface-based inversion. A high fraction of SBIs indicate that the surface is often decoupled from the atmosphere, and mixing is limited in the boundary layer. During the winter months, the SBI frequency was above 80% with decreased values into July 2011 where the SBI frequency dropped to 40%. During December 2011, the occurrence frequency was nearly 100%. The SBI occurrence values in 2010 are nearly a factor of 2 lower than 2011 for the 3 months that contain enough quality controlled profiles to display the monthly statistics; this suggests that there could be significant year-to-year variability at Summit.

[29] The monthly statistics of intensity for MWR-derived surface-based inversions, with intensity over 2°C, are depicted by box-and-whisker plots in the lower panel of Figure 6. The monthly distributions of intensity show weak inversions in June and July and transitions from (to) strong inversions in the spring (fall) in 2011. The seasonal cycle of intensity is well correlated with SBI occurrence (Figure 6). The months of June, July, and August contain an increased number of elevated inversions, despite their decreased number of overall inversions. One explanation is that incoming solar radiation leads to a warming at the surface creating turbulent mixing; hence this near-surface mixed layer would be more isothermal, resulting in an elevated inversion [*Bradley and Keimig*, 1992]. Elevated inversions that occur in the winter months, and possibly in the summer, might be attributed to mixing near the surface due to high wind speeds.

[30] Figure 7 illustrates the annual cycle of SBI occurrence and intensity from three different perspectives; 10m-2m differences from the tower measurements (red), MWR retrievals (black), and radiosonde profiles (blue). The meteorological tower is able to capture temperature changes on the order of seconds, and the MWR retrievals are sensitive to changes that occur on a time scale of hours. The radiosonde profiles are recorded twice daily and thus do not capture the entire diurnal cycle. The difference in sampling rates suggests that monthly differences in the three perspectives are expected, yet the SBI statistics among the three datasets are consistent and correlated over the course of the year.

[31] Sampling locations contribute to some of the discrepancies seen in Figure 7. Each data source is located at Summit Station, yet each is situated at different locations within the camp. The meteorological tower is located about 600 m southwest of the Mobile Science Facility (MSF) and the radiosondes are launched about 300 m northwest of the MSF. The MWR is situated on the roof of the MSF, so in actuality, the lowest values of this retrieval are well above the surface: approximately 4–5 m above the surface during summer and 2–3 m during winter due to drifting around the MSF (which is pulled out of the drift and restationed on the top of the GIS every spring). The 2m data are much closer to the actual surface temperature, yet the depth of the SBI are often much greater than 10m, explaining the depressed intensity values of the 10m–2m data (lower panel, Figure 7). The radiosonde's ability to capture the greatest vertical resolution of the SBI translates to more intermonth variability than the MWR retrievals, although

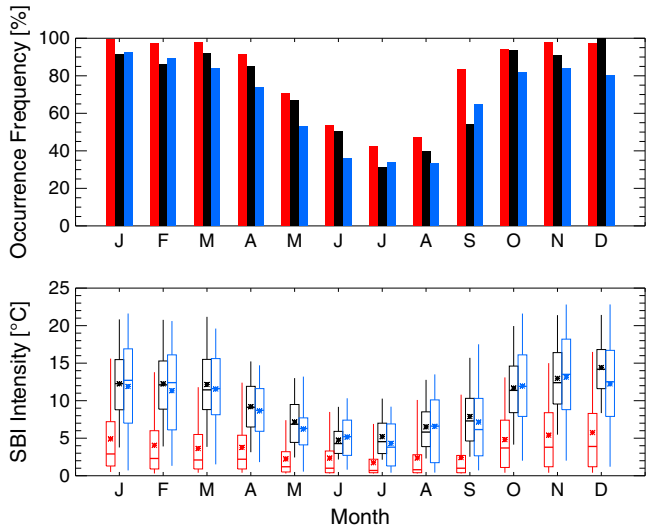

Figure 7. Fractional occurrence of surface-based inversions (top) and SBI intensity (bottom) derived from MWR (black), radiosonde (blue), and meteorological tower 10m–2m temperature difference (red). To be considered a surface-based inversion, the base must be at the surface and intensity must be greater than 2°C for the MWR and greater than 0.2°C for the radiosonde and tower temperatures. For the bottom panel, the box indicates the 25th and 75th percentiles, the whiskers indicate the 5th and 95th percentiles, the middle line is the median, and the asterisk indicates the mean.

it is striking that the MWR retrieval's median values closely track with the radiosonde values.

[32] Interannual variability related to the different subsets of data is also responsible for differences in monthly values in Figure 7. For instance, Figure 1 shows that there are very little MWR data for December 2010, and Figure 6 shows that the inversion occurrence frequency is almost 100% for December 2011. Thus, a lack of MWR sampling (due to instrument repair) during December 2010 compared with the tower and sonde statistics that include December 2010 partially explains discrepancies observed for the month of December (Figure 7).

[33] The differences in threshold values, as described in section 2.4, affect the absolute values of the occurrence frequency yet ensure that measurement error does not introduce "false-positive" inversions. The MWR-derived SBI frequency for the entire data set decreased from 78.8% to 71.8% when the threshold was adjusted from 0°C to 2°C. Changing the tower 10m–2m and radiosonde profile thresholds from 0°C to 0.2° changes the total SBI occurrence frequency from 94.8% to 80.0% and 64.9% to 64.2%, respectively.

[34] The annually evolving role of the diurnal cycle on SBI occurrence and intensity is investigated using the MWR temperature retrieval. Surface-based inversion occurrence and intensity are shown in Figure 8 using the quality controlled data from July 2011 to May 2012. The solar elevation angle (black solid contours) appears to have a large influence on the diurnal cycle, as an increased solar elevation angle corresponds to a decrease in SBI occurrence and intensity. It is evident that there is a diurnal time lag of the minimum values in Figure 8 compared to the maximum solar elevation

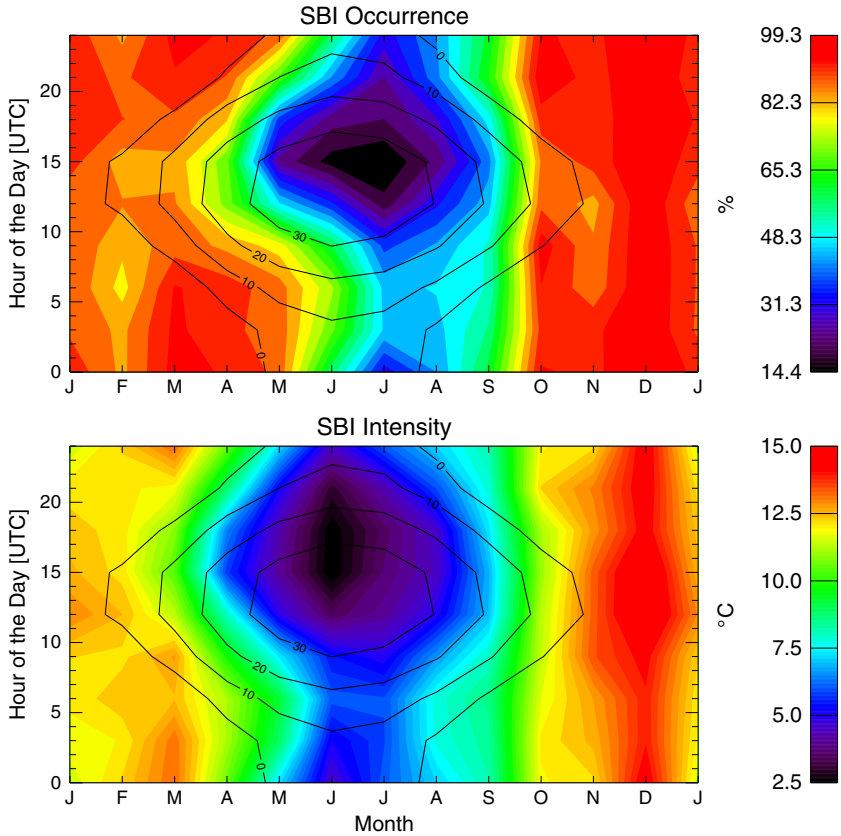

Figure 8. Data from July 2010 to May 2012, binned monthly and every 3 hours, illustrating the diurnal and annual average SBI occurrence (top) and intensity (bottom). The solid contour lines indicate the solar elevation angle (degrees).

angle; this lag could be due to the time scale of the shortwave radiative warming which acts to weaken the inversion. The top panel in Figure 8 shows that the decrease in occurrence frequency is shifted toward July and August when the solar elevation angle is decreasing, suggesting that parameters other than sun angle may also be important.

3.2. Case Study

[35] To investigate the impact of other parameters on a surface-based inversion, we analyzed a case on 20 February 2011. During this time of year, the solar influence is negligible. Meteorological tower wind speed observations, at the 10 m level, recorded a maximum wind speed of 12.4 m/s and the mean wind speed for the day of 10.3 m/s. Figure 9 illustrates the evolution of the temperature profile over the course of a 36 hour period, in addition to the associated SBI intensity, LWP, and PWV. The radiosonde temperature profiles are shown between the vertical solid lines (Figure 9, top panel) and are displayed over a 30 minute window. The first radiosonde profile in Figure 9 indicates two different inversions while the MWR-retrieved profiles, due to the decreasing resolution with height, indicate only a single inversion.

[36] The high temporal resolution of the MWR shows how the inversion responds to the presence of clouds. The LWP (Figure 9, bottom panel) and ceilometer detected cloud base heights (Figure 9, top panel) indicate that the clouds present before 0500 UTC are predominately ice. The ceilometer and data from a colocated zenith-pointing infrared spectrometer (not shown) indicate a clear sky scene at 0500 UTC, and the SBI intensity following this clear sky scene peaks at roughly 12°C. A low-level liquid-bearing cloud advects over the site at approximately 0600 UTC as indicated by increased LWP values with a peak of approximately 50 g/m^2; the cloud is about 200 m above ground level. In the presence of the liquid-bearing cloud, the intensity of the inversion decays from 12°C to below 2°C within a 2–3 hour period. At approximately 0800 UTC, the cloud base height increases, the LWP decreases, and the subsequent SBI intensity remains below 5°C until after 1900 UTC. During the period from 1200 to 1500 UTC, where the intensity strengthens from below 2°C to almost 5°C, the ceilometer is unable to distinguish cloud base height due to the cloud primarily consisting of falling ice as indicated by other instruments (not shown) such as the micropulse lidar and infrared spectrometer. From 1100 to 1900 UTC, clouds still exist for much of the time but are primarily ice. The lower troposphere above the Summit Station transitions to a prolonged clear sky scene beginning at about 1900 UTC allowing for the formation of a surface-based inversion. The radiative cooling at the surface leads to an increase of the inversion intensity as the surface temperature cools to below -50°C with the majority of cooling occurring in the lowest 50 m. As the surface is free to cool during this dry, clear period, a very intense inversion (20°C) is formed in a matter of about 10 hours.

[37] This case study serves to point out nonsolar factors that can influence surface-based inversions. Liquid-bearing clouds appear to weaken the temperature inversion by radiatively warming the surface, while low PWV and a clear sky scene

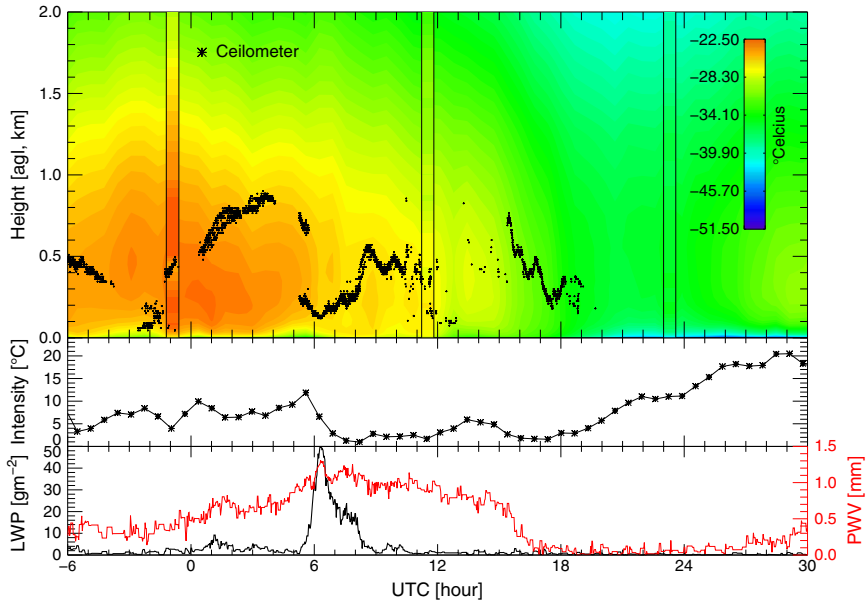

Figure 9. A case study on 20 February 2011 (±6 hours). The top panel is the MWR-retrieved temperature profiles (color) with the cloud base height as determined by the ceilometer (black dots). Three radiosonde temperature profiles are shown between the vertical solid black lines. The evolution of the intensity (middle panel) of the inversion is shown in conjunction with the liquid water path (black, bottom panel) and precipitable water vapor (red, bottom panel).

encourage SBI growth. Cloud base height could be a factor that influences SBIs, and the presence of an ice-bearing cloud seems to inhibit the formation of a strong SBI compared to clear sky scenes. Radiative heat loss at the surface is strongly modulated by the downwelling longwave radiation which reacts to factors such as low-level clouds of various types and changes to the amount of water vapor present.

3.3. Surface-Based Inversions and Liquid-Bearing Clouds

[38] There is no clear diurnal cycle for the liquid water path (not shown), but a look at the seasonal cycle of LWP is certainly warranted. The monthly statistics of LWP are shown in Figure 10, comparing the monthly distributions of liquid-bearing cloudy cases (i.e., cases where the MWR-retrieved LWP is > 5 g/m^2) versus all cases. The percentage of cases where the LWP is greater than 5 g/m^2 is indicated by the numbers at the top of Figure 10. The lack of the number of liquid-bearing clouds with larger LWP in the winter is likely due to the very cold conditions, high altitude, and the significant distance from liquid water sources; however, the summer season is warm enough to sustain clouds that contain super cooled liquid water. June 2011 has a lower fraction of liquid-bearing clouds than the months of July, August, and September, and this could explain the monthly asymmetry of the minimum SBI occurrence (July) compared to the maximum solar

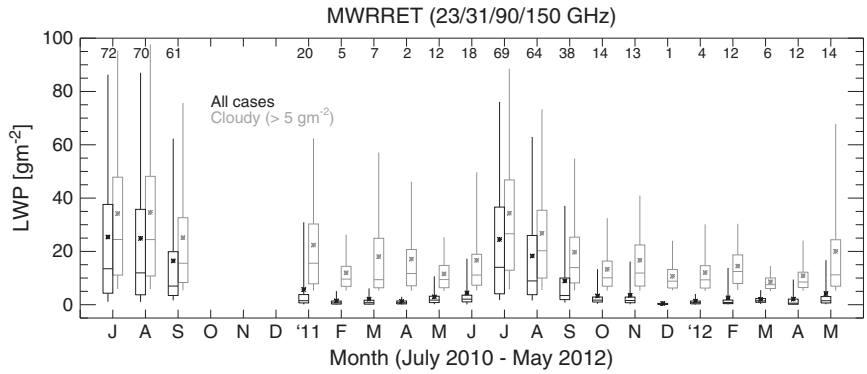

Figure 10. Liquid water path from July 2010 to May 2012 determined by the MWRRET retrieval. The monthly distributions on the left (black) are for all cases, and the distributions on the right (gray) are for the subset of cases where the LWP is over 5 g/m^2 (i.e., "cloudy"). The box indicates the 25th and 75th percentiles, the whiskers indicate the 5th and 95th percentiles, the horizontal line inside the box is the median, and the asterisk indicates the mean. The monthly percentage of cases that contain liquid water (>5 g/m^2) are indicated by the numbers at the top of the panel.

elevation angle (June) seen in Figure 8. In addition, August and September 2010 have a larger fraction of liquid-bearing clouds with higher LWP values as compared to the same months in 2011, which corresponds to lower SBI occurrence and intensities in August and September 2010 (Figures 6 and 10).

[39] Figure 10 shows that the winter months have fewer liquid-bearing clouds leading to increased surface infrared radiative cooling. The low number of liquid-bearing clouds in the winter and lack of solar radiation could be a major factor in the formation of strong inversions relative to the summer months. For instance, during the dry December 2011 with few liquid-bearing clouds, the SBI occurrence frequency is very close to 100% (Figure 6). During the summer months, the increased number of liquid-bearing clouds increase the longwave downward flux. The efficiency of surface cooling to space is limited by the opacity of the cloud, effectively weakening the inversion since the trapped energy goes toward heating the surface.

[40] Judging from the case study in Figure 9, liquid water clouds have an impact on surface-based inversions on short time scales. By taking the mean of the LWP values during a 5 minute window centered on the temperature retrieval, the relationship between SBI intensity and LWP is illustrated in the top panel of Figure 11. From 0 to 20 g/m^2, the figure shows that as the liquid water path increases, the intensity of the SBI decreases, suggesting a correlation between an increase of liquid-bearing clouds and weaker inversions. The median SBI intensities are fairly constant over the two separate ranges 20–40 g/m^2 and > 40 g/m^2 while generally maintaining decreasing intensities with increases in LWP. The mean PWV values during the same 5 minute window are shown in the bottom panel of Figure 11. SBI intensity statistics for PWV below 2 mm suggest that dry conditions correlate with stronger surface-based inversions. This correlation could be caused by the increased atmospheric transmissivity in the 18–35 μm window (e.g., *Turner and Mlawer* [2010]), associated with low PWV, which increases the radiative cooling of the surface.

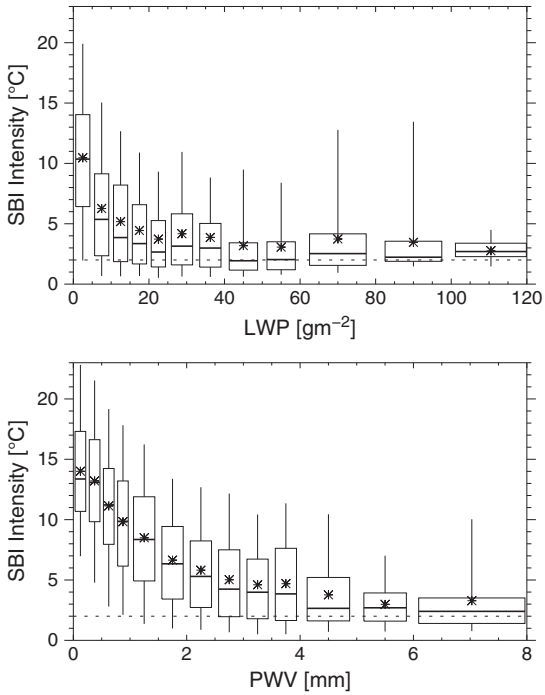

Figure 11. Surface-based inversion intensity as a function of the mean LWP (top panel) and PWV (bottom panel) over a 5 minute window surrounding the temperature retrieval for cases spanning July 2010 to May 2012. The box indicates the 25th and 75th percentiles, the whiskers indicate the 5th and 95th percentiles, the horizontal line inside the box is the median, and the * indicates the mean.

[41] To ensure that the apparent trends in Figure 11 are not caused by correlation with the annual solar cycle at Summit, Figure 12 shows the monthly median SBI intensities as a function of (a) mean LWP, (b) 10 m wind speed, (c) cloud base height, and (d) PWV over the 5 minute window. The PWV analysis only includes clear-sky scenes as determined by the ceilometer. By only using clear sky cases, the influence of PWV on SBIs is decoupled from the possible influence of clouds.

[42] For each month in Figure 12a, the LWP data shows the same correlation as that of Figure 9, namely, weaker SBI intensities with increasing LWP. The 0–5 g/m^2 bin contains the highest median SBI intensity value for each month, suggesting that clear sky scenes are conducive to the existence of stronger surface-based inversions. The annual SBI intensity cycle is evident, although the exact relationship with LWP changes with season.

[43] Additional factors are associated with surface-based inversions. Median SBI intensity is found to peak at wind speeds ranging from 3 to 10 m/s (Figure 12b). There are few cases with low wind speeds (0–2 m/s) and strong inversions, perhaps because surface-based inversions create an inversion wind [*Hudson and Brandt*, 2005]. The seasonal cycle suggests that SBIs with larger intensities are associated with stronger inversion wind speeds; however, there is a dropoff in SBI intensity above 10 m/s in all months, as very strong winds may lead to mechanical mixing that weakens the inversion at this site. Strong SBIs create conditions that are conducive for the formation of low level fog, evidenced by the strongest inversions corresponding to cloud base heights below 50 m (Figure 12c). Apart from this low-level fog, cloud bases below 1 km typically correspond to decreases in SBI intensity while at higher altitudes the cloud is likely physically too high to significantly warm the surface and weaken the SBI. Figure 12d shows that most PWV values are below 1 mm from November to February and above 1 mm from June to September. During these two periods, the SBI intensity does not seem to be dependent on PWV, although during the spring transition period (March–May), there seems to be a possible correlation of weaker SBI intensities with increasing PWV. The trend in the bottom panel of Figure 11 is likely due to the intra-annual variability of PWV and to the correlation of PWV and LWP.

[44] In general, June contains decreased SBI intensities with the least amount of variation as a function of the four factors examined in Figure 12, a phenomenon that is partially explained by the solar influence decreasing SBI intensities during this month. During the month of July, the frequency of liquid-bearing clouds increases as well as the amount of PWV, thereby increasing atmospheric opacity and the downwelling longwave radiation, effectively trapping heat near the surface. Combined with solar warming, these factors will result in weaker inversions and a general warming

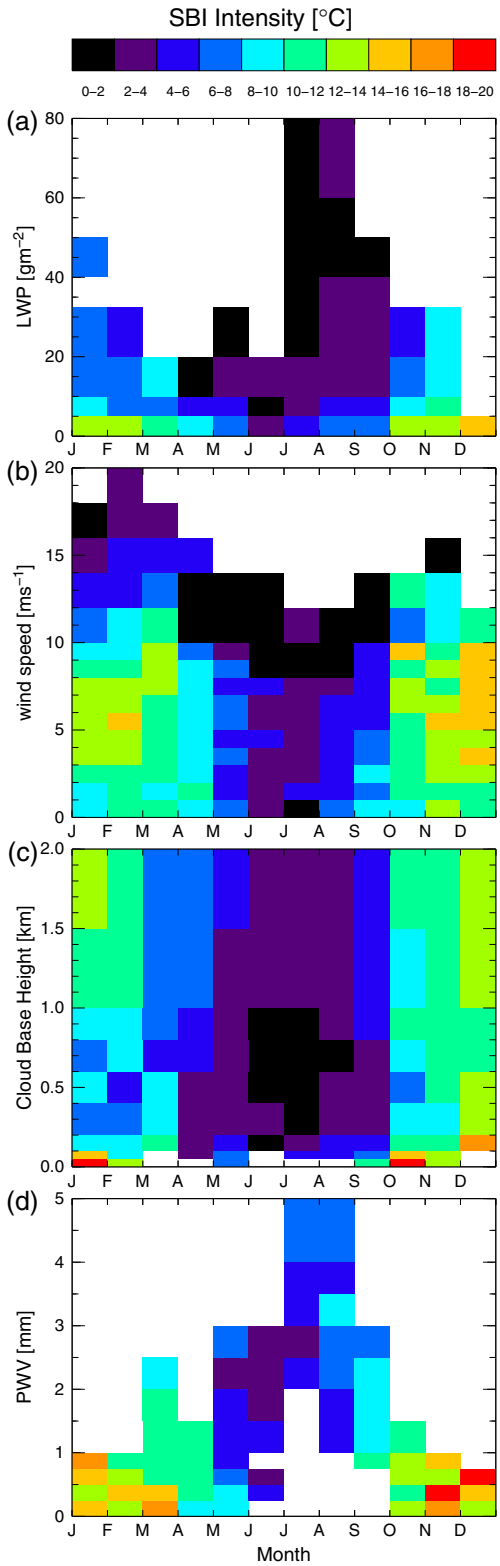

Figure 12. The monthly median SBI intensity, derived from MWR-retrieved profiles, as a function of (a) LWP, (b) wind speed, (c) cloud base height, and (d) PWV. Only cases where the ceilometer does not detect a cloud over the 5 minute window centered on the MWR temperature profile retrieval are displayed in panel (d). For each bin, a minimum of 9 cases must be present to calculate the median SBI intensity value.

of the surface layer during the summer months. Investigation of Figure 12 pertaining to the winter months suggests that low-level, liquid-bearing clouds play a role in weakening commonly occurring wintertime surface-based inversions while particularly dry and clear conditions are identified with SBI enhancement.

4. Conclusion

[45] Situated in central Greenland, Summit Station is a prime location to investigate the cloud and atmospheric properties that affect the surface energy of the GIS. The measurements taken by the suite of instruments deployed by the ICECAPS project provide a unique and comprehensive data set to study the atmospheric state above Summit Station and provide insights into the processes that affect central Greenland. While it will take a number of years and more quality controlled data from additional instruments to match the comprehensive study done on Antarctic plateau by *Hudson and Brandt* [2005], the observations at Summit provide an initial perspective on the annual evolution of surface-based inversions at this unique Arctic site.

[46] Surface-based inversions are a dominant feature above the Greenland ice sheet, creating a stable layer that limits vertical mixing and decouples the atmosphere from the surface. SBI presence and intensity are examined using complementary perspectives from MWR, radiosonde, and a meteorological tower. Nearly 72% of MWR profiles show surface-based inversions compared to 64% of radiosonde profiles and 80% as observed by meteorological tower data. Wintertime SBIs are very frequent and strong (intensity 20°C at times) because of the cold and dry atmosphere with relatively few clouds, which allows for strong radiative cooling at the surface. The transition from winter to summer sees a decrease in SBI occurrence and intensity as the surface is presumably warmed by enhanced insolation and the presence of more clouds, particularly those that are composed of liquid water. Investigation of the diurnal cycle supports the idea that these two factors play a role in the weakening of surface-based inversions. The influence of the clouds in July and August offsets the minimum SBI occurrence from the months with maximum insolation and possibly serves to dampen the diurnal cycle in September.

[47] Higher temporal sampling by the MWRs is used to study a case on 20 February 2011 where the intensity of the temperature inversion decays within a matter of hours. The decrease of SBI intensity is likely due to the presence of a liquid-bearing cloud, which limits surface radiative cooling and increases the downward longwave flux compared to the initial clear sky value. Without a temperature inversion directly above the surface, the boundary layer becomes less stable allowing for a deeper mixed layer, enhancing the interaction between the surface and the atmosphere.

[48] Since the case study suggests that the presence of liquid-bearing clouds leads to the decay of surface-based inversions while the subsequent clear sky scene leads to the formation of a stronger and deeper inversion, the dependence of SBI metrics on LWP is investigated. Increasing LWP is correlated with a reduction in the intensity of the inversion. For clear sky cases, when the LWP is $< 5\ g/m^2$, the majority of cases had a SBI intensity over 10°C.

[49] An increase in PWV, spurred by a warming climate, would reduce SBI intensities by increasing the opacity of the atmosphere. Elevated PWV amounts also create conditions conducive for more frequent cloud occurrence: ice, liquid, and mixed phase. In the presence of Arctic clouds, atmospheric opacity is greatly increased, especially for liquid-bearing clouds. Thus, a change in cloud frequency or cloud microphysics toward an increase in LWP, especially for low-altitude clouds, would lead to a reduction in the intensity of surface-based inversions with notable consequences on the surface energy balance.

[50] **Acknowledgments.** This work is supported by the National Science Foundation under Grants No. ARC-0904152, ARC-0856559 and ARC-0856773. Historical ozonesonde soundings and the near-surface meteorological tower data are provided by the National Oceanic and Atmospheric Administration's Global Monitoring Division. Top notch support was provided by Katrine Gorham, the employees of Polar Field Services, and various ICECAPS science technicians, including Lance Roth who repaired the HATPRO radiometer during December 2010. Erik Olson from the University of Wisconsin installed and maintained the microwave radiometers.

References

Bourne, S. (2008), A climate perspective of observed and modeled surface-based temperature inversions in Alaska. M.S. thesis, Dept. of Atmospheric Sciences, University of Alaska Fairbanks, 106 pp., [available online at: http://www.uaf.edu/asp/Students/theses/Bourne_SM.pdf]

Bradley, R. S. and F. T. Keimig (1992), Climatology of surface-based inversions in the North American Arctic, *J. Geophys. Res.*, *97*(D14), 15 699–15 712.

Cadeddu, M. P., G. E. Peckham, C. Gaffard (2002), The vertical resolution of ground-based microwave radiometers analyzed through a multiresolution wavelet technique. *IEEE Trans. Geosci. Remote Sens.*, *40*(3), 531–540.

Cadeddu, M. P., V. H. Payne, S. A. Clough, K. Cady-Pereira, and J. C. Liljegren, (2007), Effect of the oxygen line-parameter modeling on temperature and humidity retrievals from ground-based microwave radiometers. *IEEE Trans. Geosci. Remote Sens.*, *45*(7), 2216–2223.

Clough, S., M. Shephard, E. Mlawer, J. Delamere, M. Iacono, K. Cady-Pereira, S. Boukabara, and P. Brown (2005), Atmospheric radiative transfer modeling: a summary of the AER codes, *J. Quant. Spectrosc. Radiat. Transfer*, *91*, 233–244.

Crewell, S. and U. Löhnert (2003), Accuracy of cloud liquid water path from ground-based microwave radiometry 2. Sensor accuracy and synergy, *Radio Sci.*, *38*(3), 8042.

Crewell, S. and U. Löhnert (2007), Accuracy of boundary layer temperature profiles retrieved with multifrequency multiangle microwave radiometry, *IEEE Trans. Geosci. Remote Sens.*, *45*(7), 2195–2201.

Han, Y. and E. R. Westwater (2000), Analysis and improvement of tipping calibration for ground-based microwave radiometers, *IEEE Trans. Geosci. Remote Sens.*, *38*(3), 1260–1276.

Hudson, S. R. and R. E. Brandt (2005), A look at the surface-based temperature inversion on the Antarctic plateau, *J. Climate*, *18*, 1673–1696.

Liebe, H. J., G. A. Hufford, and T. Manabe (1991), A model for the complex permittivity of water at the frequencies below 1 THz, *Int. J. Infrared Millim. Waves*, *12*, 659–675.

Liljegren, J. C. (2000), Automatic self-calibration of the ARM microwave radiometers. Microwave Radiometry and Remote Sensing of the Environment, P. Pampaloni and S. Palencia, Eds., 433–443, VSP Press, Utrecht, The Netherlands.

Löhnert, U. and O. Maier (2012), Operational profiling of temperature using ground-based microwave radiometry at Payerne: prospects and challenges, *Atmos. Meas. Tech.*, *5*, 1121–1134.

Maschwitz, G., U. Löhnert, S. Crewell, T. Rose, and D. D. Turner (2013), Investigation of ground-based microwave radiometer calibration techniques at 530hPa, *Atmos. Meas. Tech.*, [submitted].

Mlawer, E. J., V. H. Payne, J.-L. Moncet, J. S. Delamere, M. J. Alvarado, and D. C. Tobin (2012), Development and recent evaluation of the MT_CKD model of continuum absorption, *Phil. Trans. R. Soc. A*, *370*, 2520–2556.

Payne, V. H., E. J. Mlawer, K. E. Cady-Pereira, and J. Moncet (2011), Water vapor continuum absorption in the microwave, *IEEE Trans. Geosci. Remote Sens.*, *49*(6), 2194–2208.

Rodgers, C. D. (2000), Inverse Methods for atmospheric sounding: Theory and Practice. World Scientific, 1–79 pp.

Rose, T., S. Crewell, U. Löhnert, and C. Simmer (2005), A network suitable microwave radiometer for operational monitoring of the cloudy atmosphere, *Atmos. Res.*, *75*, 183–200.

Rose, T. and H. Czekala (2009), RPG's atmospheric remote sensing radiometers. Operating manual version 8.04, Radiometer Physics GmbH, 243 pp. [www.radiometer-physics.com].

Shupe, M. D., et al., (2008), A focus on mixed-phase clouds, *Bull. Amer. Meteor. Soc.*, *89*, 1549–1562.

Shupe, M. D., et al., (2013), High and dry: New observations of tropospheric and cloud properties above the Greenland Ice Sheet, *Bull. Amer. Meteor. Soc.*, doi:10.1175/BAMS-D-11-00249.1.

Sverdrup, H. U., (1926), Scientific work of the Maud Expedition, 1922-1925, *Sci. Mon.*, *22*(5), 400–410.

Turner, D. D., R. O. Knuteson, and H. E. Revercomb (2006), Noise reduction of atmospheric emitted radiance interferometer (AERI) observations using principal component analysis, *J. Atmos. Oceanic Technol.*, *23*, 1223–1238.

Turner, D. D., S. A. Clough, J. C. Liljegren, E. E. Clothiaux, K. E. Cady-Pereira, and K. L. Gaustad (2007), Retrieving liquid water path and precipitable water vapor from the atmospheric radiation measurement (ARM) microwave radiometers, *IEEE Trans. Geosci. Remote Sens.*, *45*(11), 3680–3690.

Turner, D. D., and E. J. Mlawer (2010), The radiative heating in underexplored bands campaigns, *Bull. Amer. Meteor. Soc.*, *91*, 911–923.

Twomey, S. (1977), Introduction to the Mathematics of Inversion in Remote Sensing and Indirect Measurements, 27–149 pp, Dover Publications, Inc, Mineola, New York.

Zhang, Y., D. J. Seidel, J. Golaz, C. Deser, and R. A. Tomas (2011), Climatological characteristics of Arctic and Antarctic surface-based inversions, *J. Climate*, *24*, 5167–5186.